Electron and Ion Transport in Semi-Dilute Conjugated Polyelectrolytes: View from a Coarse-Grained Tight-Binding Model

Journal:	*Molecular Systems Design & Engineering*
Manuscript ID	ME-ART-12-2022-000285.R2
Article Type:	Paper
Date Submitted by the Author:	13-Feb-2023
Complete List of Authors:	Friday, David; University of Illinois at Urbana-Champaign, Department of Chemistry Jackson, Nicholas; University of Illinois at Urbana-Champaign, Department of Chemistry

Conjugated polyelectrolytes are an emerging class of organic mixed ion-electron conducting materials transforming modern bioelectronics. Molecular modeling efforts that facilitate molecular design of ion and electron transport in this materials class necessitate the challenging integration of techniques at multiple length scales spanning electronic degrees of freedom (quantum chemistry), nanoscale packing (atomistic molecular dynamics), and mesoscopic ordering (coarse-grained molecular dynamics). Here, we apply a novel coarse-grained model imbued with quantum mechanical prediction capabilities to explore multiscale structure formation and its impact on electron and ion transport in conjugated polyelectrolytes. This work provides the first molecular insights into structure formation and ion-electron transport in conjugated polyelectrolytes, and sheds immediate light on the nature of fiber formation in conjugated polymers and its impact on quantum mechanical delocalization. The models employed in this work hold the potential to transform the current paradigm for computational design in the complex class of mixed conducting polymers.

Journal Name

Electron and Ion Transport in Semi-Dilute Conjugated Polyelectrolytes: View from a Coarse-Grained Tight Binding Model

David M. Friday[a] and Nicholas E. Jackson,[a]

Conjugated polyelectrolytes (CPEs) are a rising class of organic mixed ionic-electronic conductors, with applications in bio-interfacing electronics and energy harvesting and storage devices. Here, we employ a quantum mechanically informed coarse-grained model coupled with semiclassical rate theory to generate a first view of semidilute CPE morphologies and their corresponding ionic and electronic transport properties. We observe that the poor solvent quality of CPE backbones drives the formation of electrostatically repulsive fibers capable of forming percolating networks at semi-dilute concentrations. The thickness of the fibers and the degree of network connectivity are found to strongly influence the electronic mobilities of the morphologies. Calculated structure factors reveal that fiber formation alters the position and scaling of the inter-chain PE peak relative to good solvent predictions and induces a narrower distribution of interchain spacings. We also observe that electrostatic interactions play a significant role in determining CPE morphology, but have only a small impact on the local site energetics. This work presents a significant step forward in the ability to predict CPE morphology and ion-electron transport properties, and provides insights into how morphology influences electronic and ionic transport in conjugated materials.

Conjugated polyelectrolytes (CPEs) are semiconducting polymers characterized by a π-conjugated backbone and non-conjugated side chains bearing pendant ionic groups.[1] This combination of molecular features imparts both optoelectronic functionality and solubility in polar media, enabling applications including chemical and biological sensors, biological imaging, and orthogonally soluble interfacial materials.[2–4] Moreover, these molecular attributes facilitate simultaneous electronic and ionic conduction in a single phase, making CPEs an important material class within the field of organic mixed ion-electron conductors (OMIECs) that are beginning to transform bioelectronics.[5–8] This combination of functional attributes sits at the intersection of the relatively mature fields of electron and ion transporting polymers, but cannot benefit from the naïve application of pre-existing design rules from either field due to the strong coupling between electronic and ionic degrees of freedom.[9]

Experimental work on semidilute CPEs has existed for over a decade, providing nascent structure-function relationships that are the foundations for molecular design strategies. The semiflexibility and hydrophobic character of CPE backbones strongly impact their morphologies, producing long cylindrical aggregates

or micelles at low concentrations.[10,11] For rigid CPE backbones, these micelles can become effectively crosslinked via poor-solvent interactions, forming hydrogels at concentrations as low as 1% w/v,[12–14] with longer chain lengths improving the percolation and electronic conductivity of these networks.[15,16] More flexible CPEs (e.g. thiophene) tend to be deposited as thin films that swell in ambient humidity.[17] Solvent can further alter the nature of CPE aggregation, producing random coils in good solvents or self-assembled micelles in poor solvents,[10] and can be used to anneal a morphology to improve conductivity.[12] In addition to the CPE backbone, longer side chains have recently been shown to improve both the ionic and electronic conductivity of thiophene-based CPEs across a range of hydration levels.[16] The larger ionic conductivity is likely due to the more flexible side chains facilitating the motion of counterions,[18,19] while the higher electronic mobility is due to reduced swelling, making the CPE network more strongly connected and increasing electronic conductivity, especially at high water content (50-80% w/v). When hydrated, the pendant ions of CPEs are capable of electrostatically stabilizing charge carriers on the backbone due to the dissociation of the counterions into solution.[16] These works delineate how molecular structure impacts physical properties of CPEs, but are limited in their ability to attribute the mechanisms by which molecular structure influences morphology, or how the interplay of CPE chemical structures impacts their final mixed conducting proper-

a Department of Chemistry, University of Illinois at Urbana-Champaign, Urbana, Illinois 61801, United States; jacksonn@illinois.edu.

ties. To these ends, CPEs are poised to benefit from scalable computational models capable of unearthing molecular scale insights at the nexus of morphology and mixed conduction.

A small number of emerging theoretical studies have begun to characterize how backbone chemistry and ion identity influence electronic properties of CPEs. DFT studies of donor-acceptor CPEs have shown that ionic functionalities have little impact on the HOMO-LUMO gap,[20] a small (0.1 to 0.01 eV) effect on the positive polaron binding energy,[21] and a negligible impact on optical absorption.[22] A study combining MD and NMR data showed that small metal ions tend to bind to pendant carboxylate groups, while only large ions (Cs^+ or Tetra-alkyl-amines) interact directly with a thiophene backbone.[23] The small amount of theoretical work attests to the difficulty of modeling CPEs, particularly at the mesoscopic length scales that dictate morphology formation. As such, there is a critical needs in the modeling of CPEs for computational models capable of accessing experimentally relevant length scales while maintaining molecular descriptors of electronic structure.

The development of structure-function relationships in CPEs is complicated by the complex interplay of interactions at multiple length scales. Conformationally, CPEs represent the intersection of semiflexible polyelectrolyte physics with the strongly interacting anisotropic π-electron systems characteristic of organic semiconductors. Simultaneously, these conformational predictions must be integrated into molecularly-specific QM analyses of electron transport at the 10-100 nm scale. While established quantum chemical methods can predict the electronic structure of organic semiconductors with high precision,[24] the large length scales of CPEs, along with the need for conformational averaging of the statistical ensemble, makes these methods computationally intractable for the systems targeted in this work. Furthermore, the accuracy of these quantum chemical methods may be compromised in this work by intrinsically ill-defined atomistic backmapping, bias induced by using Bloch's theorem on a system that is not truly periodic, as well as the limited ability of DFT to accurately model the heterogeneous water interfaces surrounding CPEs.[25] These factors challenge the use of any single molecular modeling methodology, with high-fidelity treatments necessitating expensive multiscale workflows.[26] In these efforts, coarse-grained (CG),[27–32] all-atom (AA),[33–36] and quantum chemical (QC)[37–41] simulation methods are employed in concert to tackle phenomena at a variety of scales in conjugated materials.

To these ends, significant work has been conducted to understand the morphology and function of PEDOT:PSS films using molecular modeling.[42–46] Recently, our group has advanced a QM-informed anisotropic CG model targeted specifically at understanding both conformational and electronic structure of CPEs.[47] In these efforts, a tight-binding Hamiltonian is endowed with configurational dependence parameterized by the anisotropic degrees of freedom in the CG model. Solvent quality, chain stiffness, dihedral disorder, and explicit electrostatics are all built into the CG model and influence the associated electronic structure of the chains. This model enables a rapid characterization of qualitative electronic structure changes at length scales inaccessible via conventional QC or AA modeling.

In previous work, we have employed QM-informed CG models to understand the conformational and electronic structure relationships of dilute CPEs.[47] Single chain conformations of polythiophene-like CPEs were explored as a function of solvent conditions and chain stiffness, producing a hierarchy of rod-like, racquet, pearl necklace, and helical conformations. Electronic structure analysis was performed for each conformational archetype using a tight-binding Hamiltonian, for which electrostatics was observed to influence electronic structure in CPEs primarily as a modulator of accessible conformations, and only minimally by affecting on-chain site energies. Proxies for QM transport were computed using the thermal Green's function from which it was observed that electron transport should be most efficient in the helical and racquet conformations, which was attributed to flattened dihedrals and large through-space couplings within the collapsed conformations. Interestingly, kink formation within racquets of CPEs was not observed to significantly deteriorate electronic conjugation. The integration of these insights forms the first multiscale understanding of structure-function relationships in CPEs, and motivates further understanding at higher concentrations (e.g. hydrogels, swollen films) relevant to practical device applications.

In this paper we demonstrate how QM-informed CG models for polymeric materials can be employed to design mixed electron-ion conduction in CPE systems at the molecular scale. First, we detail the anisotropic CG model and coupled tight-binding Hamiltonian used to generate our results, along with the simulation conditions and protocols used to equilibrate morphologies. Next, we describe our methods for computing ionic and electronic transport, include the coupling of a tight-binding Hamiltonian to semiclassical rate theories and mean-field solutions of a master equation, from which electronic mobilities are derived. We then explore the morphology, ionic transport, and electronic transport of hydrophobic and hydrophilic CPEs as a function of concentration. Specifically, we observe how the balance between poor-solvent aggregation and electrostatic repulsion determines the thickness of CPE fibers and the connectivity of the morphology that underpins electron transport. We then predict the electronic and ionic transport properties of CPEs, revealing how both local structure (e.g. fiber thickness) and global structure (e.g. network connectivity) impact charge mobility in CPEs. These results outline how experimentalists can leverage variations in CPE concentration and solvent quality to engineer the morphologies, ionic conductivities, and electronic conductivities of molecular CPE systems. Of particular interest is the predicted ability to engineer the electronic conductivity of mixed conducting CPEs independently of the electronic conductivity, facilitating molecular systems design. We conclude with a discussion of future directions for the multiscale modeling of OMIECs, specifically CPEs.

1   Methodology

1.1   Coarse-Grained Model

The CG CPE model is described in previous work[47] and summarized briefly here. The CPE model is based on a P3ImHT-Br 64-mer in a semidilute solution. Each monomer contains
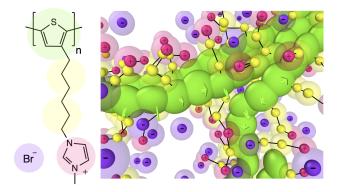
Fig. 1 Coarse-grained poly[3-(6-imidazoliumhexyl)thiophene] bromide (P3ImHT Br) and a representative snapshot of a poor-solvent morphology. Anisotropic backbone beads are green, with green arrows representing the orientation of the vector normal to the π-electron system of the backbone beads. Side chain beads are yellow, cationic pendant charges are pink, and anionic counterions are purple. Semi-transparent boundaries are LJ radii, and bonds are black lines.

an anisotropic Gay-Berne (GB) bead representing thiophene and isotropic Lennard-Jones (LJ) beads representing the hexyl side chains, imidazole pendant cation, and the bromide counter-anion (Figure 1). All simulations are performed in LAMMPS.[48] The solvent (water) is treated implicitly with renormalized short-range intermolecular interactions, a modified dielectric constant, and a Langevin treatment of the solvent dynamics.[48–50]

Intermolecular pair interactions were chosen to drive chain aggregation via anisotropic π-stacking. To control solvent quality, the well depth of the GB interaction between monomers was set to 3 k_BT / 0.3 k_BT between monomers in the π-stacking (ε_{GB}) direction and 1 k_BT / 0.1 k_BT in the orthogonal directions for poor/good solvent conditions, respectively. All LJ well depths (ε_{LJ}) corresponding to isotropically interacting beads were set to 0.1 k_BT in all simulations. Charges of +1 / -1 were placed on the imidazole pendant cation and bromide counter anion beads, respectively, with their interactions mediated by a dielectric constant of 1 in reduced units, corresponding approximately to the dielectric of water.

All two-body bonded interactions were harmonic, with LJ beads bonding between centers of mass, and anisotropic GB beads bonding between rigidly bound off-center massless ghost particles, allowing bonded beads to apply a torque to the backbone. The three-body angle interactions were modeled as harmonic, with an angle constant of 1 k_BT for the side chains, and 6 k_BT for the backbone to capture the expected persistence lengths.[51] The dihedral angles between the π-systems of anisotropic backbone beads were modeled using an OPLS style dihedral with $K_2 = 2.4\ k_BT$.[52]

Generating an equilibrated semidilute CPE morphology is a non-trivial undertaking, especially under poor solvent conditions, due to the long timescales of relaxation. Experimental work has shown that CPE films generated from fresh dilute solutions can have charge mobilities twice that of films generated from 1-month aged dilute solutions,[17] making complete equilibration using molecular modeling impractical. To explore the possible

morphologies formed by the CG CPE model, three sets of independent simulations were run at concentrations of 10, 15, 20, 30, 40, and 50% w/v. For reference, 10% w/v is equivalent to 0.115 beads/σ^3, 0.023 monomers/σ^3, or 0.31 M. In these simulations, 1 k$\tau \sim$ 2 ns in real units, although CG dynamics are not expected to agree quantitatively with all-atom dynamics. These three sets of simulations span the conditions of a CPE in good solvent, poor solvent with maximized inter-chain connections (quenched), and poor solvent with reduced inter-chain connections (compressed), as shown in Figure 2 and described in detail below.

Good Solvent: A system of 100 CPE chains in good solvent ($\varepsilon_{GB} = 0.3\ k_BT$) was initialized as a two dimensional array of parallel chains, and relaxed for 100 kτ at 6% w/v. The simulation box was then compressed to 50% w/v over 47 kτ (1 kτ per %w/v after 10%w/v), with final configurations saved at the six desired concentrations. Each of the six snapshots were then run for a 50 kτ ($\sim$100 ns) production run.

Poor Solvent, "Quenched" (maximized inter-chain connections): The six snapshots representing the CPE in good solvent were used as the initial configurations for quenched poor solvent simulations ($\varepsilon_{GB} = 3\ k_BT$). In these simulations, all polymers π-stacked with their nearest neighbors, forming a single network in < 2 kτ. This process can be thought of as an instantaneous 'solvent quenching' of the morphology, maximizing inter-chain connections. Each of the simulations were relaxed for 100 kτ ($\sim$ 200 ns), followed by a production run of 50 kτ. In more dilute solutions (10-20% w/v), the combined effect of electrostatic repulsion between chains and poor solvent attraction between monomers, resulted in some chains separating from the largest network as the morphology relaxed.

Poor Solvent, "Compressed" (with reduced inter-chain connections): To simulate a morphology generated by compressing a CPE in poor solvent, the 6% w/v good solvent morphology was instantaneously quenched into poor solvent (yielding small clusters of 1-5 aggregated chains), relaxed for 8 kτ, and compressed to 50% w/v over 47 kτ by reducing the simulation box size. This is loosely analogous to evaporative concentration of the morphology. The morphologies were saved at the six selected concentrations and relaxed for 100 kτ ($\sim$ 200 ns), followed by a production run of 50 kτ.

The relaxation of the CPE simulations was monitored via several time correlation functions and the time-dependent convergence of system properties, described in detail in the Supporting Information (Figure S1). The time correlation functions showed decorrelation times < 100 kτ for the radius of gyration and the fiber thickness (described below) indicating the morphologies in the production runs are not well correlated to each other. All poor solvent simulations showed a continual increase in the average persistence length and the total GB intermolecular binding energy suggesting that the true equilibrium morphology likely contains straighter chains and thicker fibers than achieved by these simulation. This equilibrium may be similar to rigid micelle-like structures observed in dilute experimental CPE work.[12] The kinetic trapping of conjugated polymers into fiber-like morphologies has recently been proposed to explain unusual time-dependence of solution-phase SAXS data, and represents an unavoidable reality
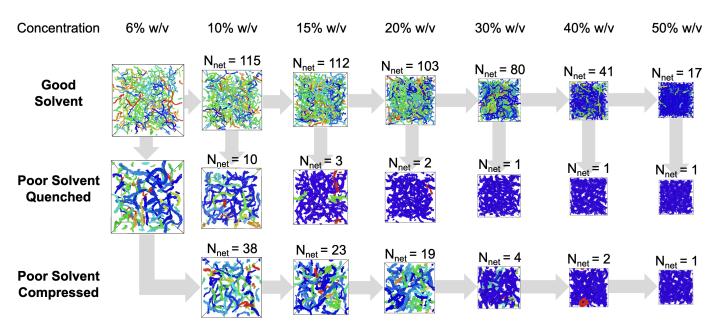
Fig. 2 CPE morphology generation scheme. Each simulation contains 100 64-mer CPE chains, and chains in the same electronic network (see Methodology) are given the same color. All simulations are derived from the 6% w/v good solvent simulation following the gray arrows. Images with labeled number of networks (N_{net}) have been relaxed for 150 kτ

of conjugated polymer simulations.[53]

1.2 Quantum Mechanical Model Hamiltonian

The electronic structure of the CPE systems were modeled using a tight-binding Hamiltonian described previously.[47] The Hamiltonian is built in a basis of monomer highest occupied molecular orbitals (HOMOs) (Eq 1). For a given configurational snapshot, the Hamiltonian is parameterized in the following manner. The on-site (diagonal) energy of each orbital is computed using the electrostatic potential on each backbone bead derived from the Ewald summation in the CG morphologies. The through-bond electronic coupling between bonded backbone beads is calculated with a cosine power series of the dihedral angle between successive monomers fitted to DFT (Eq 2).[54] Lastly, through-space nonbonded electronic couplings are modeled as an exponential decay with intermonomer distance, multiplied by angular terms to ensure electronic coupling is maximized when two backbone beads' π-systems are aligned and parallel, and zero when the π-systems are perpendicular (Eq 3), where $\alpha = 1\ \sigma^{-1}$, $r_0 = 0.75\ \sigma$, and $J_{inter} = 0.1 eV$. This represents a qualitative approximation to the real electronic coupling surface.[55,56] All constants are the same as in previous work.[47] The system's molecular orbitals (MOs) were generated from the Hamiltonian's eigenvectors. To characterize the electronic structure of the system, the density of states (DOS) of molecular orbitals and the inverse participation ratio (IPR, Eq 4) were calculated for each trajectory snapshot, where c_{nj} is the coefficient of the jth eigenvector on the nth monomer. In all following equations, monomers are represented by indices n and m, while MOs are represented by indices i and j.

$$H_{n,m} = \begin{bmatrix} V_1 & t_{1,2} & w_{1,3} & \cdots & & w_{1,N} \\ t_{1,2} & V_2 & t_{2,3} & & \ddots & \vdots \\ w_{1,3} & t_{2,3} & V_3 & & \ddots & w_{N-2,N} \\ \vdots & \ddots & \ddots & & \ddots & t_{N-1,N} \\ w_{1,N} & \cdots & w_{N-2,N} & t_{N-1,N} & & V_N \end{bmatrix} \quad (1)$$

$$t_{n,n+1} = \sum_{i=1}^{5} C_i cos^i(\phi_{n,n+1}) \quad (2)$$

$$w_{n,m} = J_{inter}(\hat{f}_n \cdot \hat{r}_{nm})^2 (\hat{f}_m \cdot \hat{r}_{nm})^2 (\hat{f}_n \cdot \hat{f}_m)^2 e^{-\alpha(|r_{nm}|-r_0)} \quad (3)$$

$$IPR_j = \left(\sum_n c_{nj}^4 \right)^{-1} \quad (4)$$

1.3 Electronic Transport

To compute the electronic conductivity as a function of morphology, the eigensystem of the tight-binding Hamiltonian parameterized from the CG configuration was used to compute electron hopping rates with a method based on work by Troisi and Fornari.[57,58] The hopping rate (k_{ij}) between any two MOs was calculated according to Eq 5, where V_{ij} is the electronic coupling between MOs, $\hbar$ is the reduced Planck constant, λ_{ij} is the reorganization energy, $k_B T$ is the thermal energy (T = 300 K), ΔE_{ij}

is the change in energy from state i to j, R_{ij} is the distance from the wavefunction centroids of state i and state j projected in the direction of the electric field, and F is the electric field strength (1e-5 eV/σ or $\sim$ 200 V/cm). The reorganization energy (λ_{ij}) is calculated according to Eq. 6, where c_{ni} is the coefficient of MO i on monomer n and the reorganization energy of a single monomer, λ_1, is 0.45 eV.

$$k_{ij} = \frac{\langle V_{ij}^2 \rangle}{\hbar} \sqrt{\frac{\pi}{\lambda_{ij} k_B T}} exp \left(\frac{-(\lambda_{ij} + \Delta E_{ij} + R_{ij}F)^2}{4\lambda_{ij} k_B T} \right) \quad (5)$$

$$\lambda_{ij} = \lambda_1 \sum_n c_{ni}^4 + c_{nj}^4 \quad (6)$$

To calculate the electronic coupling between two MOs $\langle V_{ij}^2 \rangle$, we generalized the approach of Fornari (Eq 7),[57] to allow for coupling between non-bonded monomers. This method computes a time-dependent coupling between the system's eigenstates due to dynamic disorder in intermonomer electronic couplings. We assume that this perturbation is proportional to the static electronic coupling between monomers multiplied by a fluctuating term, $V_{nm}(t) = V_{nm}\gamma_{nm}(t)$, where V_{nm} is the intermonomer electronic coupling (H_{nm}, Eq 1 with diagonals set to zero). The thermal moments of the coupling are characterized by $\langle \gamma_{nm}(t) \rangle = 0$ and $\langle \gamma_{nm}^2(t) \rangle = G^2 V_{nm}^2$, where $G = 0.005$. When the electronic coupling between monomers is squared (Eq 8), the number of terms in the summation is also squared. However, only the terms where $n = n'$ and $m = m'$ survive time averaging (Eq 9) based on the assumption that fluctuations between all pairs of different monomers are decorrelated[57] ($\langle \gamma_{nm}(t)\gamma_{n'm'}(t) \rangle = 0$ if $n \neq n'$ and $m \neq m'$).

$$V_{ij}(t) = \langle \Psi_i | V(t) | \Psi_j \rangle = \sum_{n,m} c_{in} c_{jm} \langle n | V(t) | m \rangle$$
$$= \sum_{n,m} c_{in} c_{jm} V_{nm} \gamma_{nm}(t) \quad (7)$$

$$V_{ij}^2(t) = \sum_{n,m} c_{in}^2 c_{jm}^2 V_{nm}^2 \gamma_{nm}^2(t) +$$
$$\left(\sum_{n,m} c_{in} c_{jm} V_{nm} \gamma_{nm}(t) \right) \left(\sum_{n' \neq n, m' \neq m} c_{in'} c_{jm'} V_{n'm'} \gamma_{n'm'}(t) \right) \quad (8)$$

$$\langle V_{ij}^2(t) \rangle = \sum_{n,m} c_{in}^2 c_{jm}^2 V_{nm}^2 \langle \gamma_{nm}^2(t) \rangle$$
$$= G^2 \sum_{n,m} c_{in}^2 c_{jm}^2 V_{nm}^2 \quad (9)$$

A necessary condition for the assumption of non-adiabatic incoherent hopping is that $\langle V_{ij}^2 \rangle << \lambda_{ij}^2$,[57] which is found to be true for all systems studied in this work (max observed $\langle V_{ij}^2 \rangle \sim 10^{-2} \lambda_{ij}^2$).

From the calculated rates (k_{ij}), the population of holes existing in each molecular orbital (P_i) was solved with an iterative approach[57,59] briefly summarized here. The population of holes was initialized with a Boltzmann distribution and each state's population was individually updated according to Eq 10, followed by renormalizing the total population to the targeted number of holes. This process was iterated until convergence (change in P_i < 1e-8 (10 dopants) or P_i < 1e-9 (1 dopant) per iteration for all monomers). To accelerate the calculations, only the lowest 1000 MOs were used in the mobility calculation. Several test cases were run with 3200 MOs, confirming that the truncated basis of MOs had < 2% impact on the calculated average mobility.

$$P_i = \frac{\sum_j k_{ji} P_j}{\sum_l \omega_{il}} \bigg/ \left(1 - \frac{\sum_j (k_{ij} - k_{ji}) P_j}{\sum_l k_{il}} \right) \quad (10)$$

After the MO populations had converged, the mobility was calculated according to Equation 11, where N_{dop} is the number of doped charge carriers in the system. For each morphology (good, quenched poor, compressed poor), the mobility along the x, y, and z-axes were calculated for 51 snapshots, each separated by 1 kτ of simulation time.

$$\mu = \frac{1}{FN_{dop}} \left(\sum_{ij} k_{ij}(P_i)(1 - P_j)R_{ij} \right) \quad (11)$$

While this iterative approach was generally effective, when a morphology is not well connected (e.g. at 10% w/v) the hopping rates are much smaller, and convergence can be slow. The calculated mobilities of a few snapshots, particularly those at low concentrations, exhibited non-physical negative mobilities, or anomalously high mobilities (> six standard deviations above the mean). These snapshots were removed from averaging. In the case of 10% w/v simulations, 5-25 snapshots were removed. For all other morphologies, at most five snapshots were removed from averaging. While the calculated mobilities varied greatly from snapshot to snapshot (with a standard deviation of 30 - 150% of the mean), in each simulation the average mobility along each axis varied by < 25%, indicating that adequate averaging had been performed and that the morphologies were isotropic from the perspective of electron transport. Therefore the final reported mobilities are averaged over results independently obtained along the x, y, and z axes.

The mobility of holes in a conjugated polymer network depends on both the number of holes and the electric field strength.[60] In this work, the low-field mobility was calculated for systems with low doping (1 or 10 holes, $\sim$0.016% or $\sim$0.16% doped respectively). The assumption that a field strength of 1e-5 eV/σ is in the low field limit was verified for several conformations run at 1e-7 eV/σ, showing an average 0.3% change in mobility. Using a larger field strength allowed for faster population convergence. The reported mobilities assume no hole-hole interactions (valid for low charge density system), and no anion-hole interactions (valid for high dielectric solvents, high degree of delocalization,

and high density of charged species).

2 Results and Discussion

2.1 Concentration And Solvent Dependent Morphology

In good solvent, the partial structure factor of the CPE backbone beads (Figure 3a) agrees with previous simulations of polyelectrolytes in good solvent, with the structure factor showing a strong peak that shifts to higher q and decreases in intensity with $\rho^{1/2}$ in agreement with scaling theories. [61,62] This peak is due to the electrostatic repulsion of chains that results in narrow distribution of distances between monomers of adjacent CPE chains. [63] In all CPE simulations, no low-q PE peak was observed in the structure factor, consistent with the shorter length scales accessible via molecular simulations. [61,62]

In stark contrast to good solvent, poor solvent CPE simulations form a 3-dimensional network of mutually avoiding CPE fibers (see SI for a .trj file of a morphology that can be opened in Ovito [64]). The partial structure factor of the backbone beads reveals a sharp CPE peak with a second peak at $\sim$1.8 times the primary PE peaks' position (Figure 3b). The increased sharpness of the peak in poor solvent agrees with previous SANS studies comparing poor and good solvent CPEs. [65] The appearance of a secondary peak is in further agreement with SANS data from a PCPDTBT-based CPE. [13] The high-q peaks in the structure factor correspond to monomer bond length ($\sim 0.9\sigma$) and the π-stacking distance ($\sim 1.1\sigma$). Across all q values, the only significant difference between the quenched and compressed poor solvent partial structure factors was the compressed morphology had a deeper trough between the π-stacking peak and CPE peaks than the quenched morphology (Figure S2). This result is presumably due to fewer, thicker fibers in the morphology (see below). The insensitivity of the structure factor to morphological changes between the quenched and compressed systems highlights the critical value of molecularly detailed simulations when interpreting CPE morphologies, particularly for comparison to experiments.

The low-q peaks in the structure factor suggest a highly ordered, fiber-like structure intermediate between a 2d hexagonal crystal structure and a 1D lamellar structure. To better characterize the low q structure of poor solvent simulations, the partial structure factor was fitted to the sum of two Lorentzian peaks and a low-q decay (Eq 12) as previously used to fit CPE scattering profiles. [13] In this equation, A, B, and C are the magnitude of each component of $S(q)$, n and m are the scaling exponents for the low-q decay and first peak, respectively, q_1 and q_2 are the positions of the first and second peak, respectively, and L_1 and L_2 are the length scales associated with the order of the first and second peak, respectively. The fitted values are presented in Figure S3. The ratio of primary and secondary peak positions (q_2/q_1) smoothly increases from 1.75 to 1.88 as the concentration increases from 10% to 50% w/v (Figure S4). These ratios fall within the expected ratios for a higher-order harmonic of a 2D hexagonal crystal structure ($\sqrt{3} = 1.73$) and a 1D crystal harmonic (2.00). To the author's best knowledge, this is the first assignment of a harmonic peak in a modeled CPE structure factor, providing a potential alternative interpretation of the SANS

peaks observed in a similar CPE system. [13,14] Note that when side chain beads are included in the structure factor, the harmonic peak becomes much less distinct (Figure S5).

$$I(q) = \frac{A}{q^n} + \frac{B}{1 + (|q - q_1|L_1)^m} + \frac{C}{1 + (|q - q_2|L_2)^2} \quad (12)$$

The scaling of the poor solvent CPE peak deviated from good solvent scaling theories due to the formation of multi-chain fibers in poor solvent. In poor solvent, the increase in concentration coincides with a decreasing number of independent fibers of increasing thickness. The primary peak's position scaled as $\rho^{\sim 0.3}$ and its intensity remained nearly constant (Figure 3 and S6) with respect to concentration. The sub 1/2 scaling exponent of the PE peak can be explained by the thickness of the CPE fibers increasing with concentration (see below), producing larger inter-fiber separations. These thicker fibers also increase the amplitude of the density fluctuations, producing deviations from the expected -1/2 peak intensity scaling relationship. This 0.3 scaling relationship is similar to that predicted by pearl-forming flexible PE chains in poor solvent, [66] but this relationship has not been studied in fiber-forming semi-flexible chains and presents a critical gap in our theoretical understanding of poor solvent CPEs. It should be noted that at high concentrations, the regular spacing between CPE fibers in poor solvent simulations is likely enhanced by the excluded volume of the good-solvent side chains, as the spacing between backbone fibers approaches twice the chain length.

To complement the global characterization of morphology via the partial structure factor, we also examined the CPE fiber thickness as a function of concentration and solvent quality. The distribution of fiber thicknesses is hypothesized to have a strong effect on molecular orbital delocalization and the connectivity of the charge transport network, both of which could improve electronic mobility. An algorithm was developed to determine the thickness of a CPE fiber, described in the SI. A representative result of this algorithm is shown in Figure S8. In this work, "thickness" is used to quantify the number of chains characterizing the width of a fiber, not a physical distance.

Figure 4 shows that both the average fiber thickness and the width of the fiber thickness distribution increase with concentration in poor solvent conditions. Interestingly, both the quenched and compressed simulations exhibit very similar fiber thicknesses, especially at low concentrations. It was also observed that the fiber thickness increases linearly with concentration up to 30% w/v (compressed) or 40% w/v (quenched). Using a linear fit of this data ($R^2 > 0.998$), the extrapolated fiber thickness in the dilute limit (0% w/v) is 2.05-2.08. This result is consistent with previous work which observed a fiber thickness of two in the dilute limit resulting from self-aggregation of single chains. [47]

The thickness of a fiber results from the balance of the poor solvent quality, favoring aggregation, and the electrostatic repulsion between chains, disfavoring aggregation. As the concentration of CPE increases, the free volume of the system decreases, increasing the proximity of counterions to the chains, screening the electrostatic repulsion between the pendant counterions, and allowing solvent quality to drive further aggregation. Further-
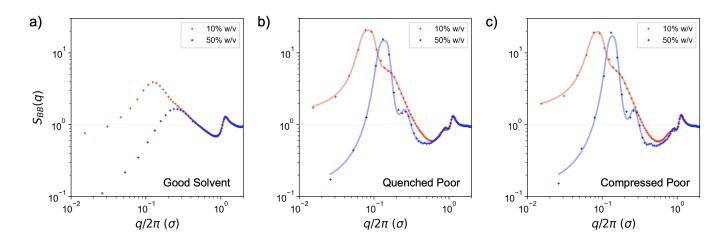
Fig. 3 Partial structure factor of the CPE backbone beads in (a) good solvent, (b) poor solvent quenched, and (c) poor solvent compressed at concentrations of 10 (red) and 50% (blue) w/v. The poor solvent data was fit to Equation 12. Values of q are divided by 2π to aid interpretation, and 1 $\sigma \sim 0.5$ nm in real space.
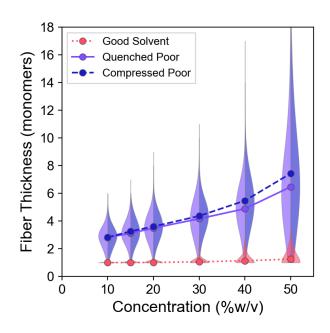

Fig. 4 Fiber thickness for good solvent and quenched/compressed poor solvent morphologies. Curves represent the distribution of fiber thicknesses and points represent the average fiber thickness.

more, the low free volumes of the morphology at higher concentrations also favor efficient packing of the anisotropic beads via π-stacking. This packing effect may explain the deviation of fiber thickness from the linear trend at $\geq 40\%$ w/v. The differences between the quenched and compressed poor solvent simulations are most likely due to kinetic trapping, as previously discussed.

2.2 Concentration Dependent Network Connectivity

In addition to characterizing the average structural properties of the CPE morphologies, the fine details of the CPE network structure are equally important in characterizing the associated electron[67] and ion[68] transport of a system. To determine the net-

work structure of a CPE morphology, an unweighted adjacency matrix between anisotropic monomers was generated by defining any two monomers with electronic coupling > 0.02 eV as adjacent to each other. This threshold preserves through-bond connections when the dihedral angle is less than $80°$, and preserves through-space connections up to 2.3 σ for monomers with perfectly aligned π-systems. The adjacency matrix was then subdivided via a crawling algorithm, similar to previous work.[67] The number of networks and the size of the largest network for each snapshot were recorded over time (Figure S9), and the robustness of number of networks to the electronic coupling threshold is shown in Figure S10.

Despite the nearly identical structure factors and fiber thickness distributions of the quenched and compressed poor solvent simulations, Figure 5 shows significant differences in their corresponding network structures. As described previously, the quenched poor solvent simulations were designed to probe the limit of a network maximizing interchain connections, while the compressed poor solvent simulations were designed to generate a network favoring intrachain π-stacking. This approach successfully produced fewer separate networks in the quenched morphology at all concentrations, with the largest network spanning >50% of the monomers for all morphologies (Fig S10). In contrast, the compressed simulations generated a distribution of smaller, isolated networks at concentrations < 30% w/v, and a single nearly percolative network at $\geq 30\%$ w/v. These granular details of the network structure manifest important difference in the resulting electronic mobilities of the different CPE systems. Additional visualizations of the morphologies are provided in the SI (Figure S11) using the UMAP (Uniform Manifold Approximation and Projection) algorithm.[69]

2.3 Concentration Dependent Electronic Transport

With the concentration dependent morphologies of CPEs characterized, we next explore how the morphology impacts the energies and delocalization of the highest lying HOMOs, and how the
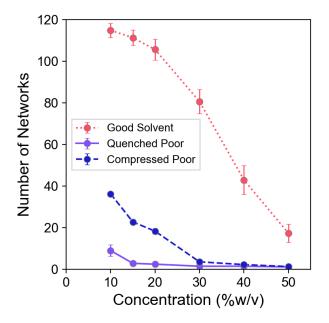
Fig. 5 Number of networks vs CPE concentration. Each point is averaged over 50 kτ. Error bars represent one standard deviation. The threshold electronic coupling value for two monomers being connected is 0.02 eV

electron hopping rates determine the bulk electronic mobility.

A hallmark of CPEs is that ions are chemically attached to the semiconducting backbone, prompting interest in what direct effect these ions and their counterions have on the electronic properties of the polymer. Similar to dilute CPEs,[47] the standard deviation of the on-site electrostatic potential was less than 0.011 eV for all systems (Figures S12 and S13). To assess what role additional disorder not included in our model (e.g. solvent polarization) might have on the system's electronic structure, a Gaussian-distributed random disorder was applied to each monomer with a standard deviation of 0.1 eV; this disorder did not qualitatively impact the electronic structure differences between systems (Figure S14). These results reinforce that electrostatic disorder has a small influence on the electronic structure of CPEs in the dilute and semi-dilute regimes for the dielectric (water) studied here. One anticipated result from the electrostatic analysis is the observation that the 10% w/v poor solvent morphologies have a +0.014 eV average electrostatic potential compared to the 50% w/v morphologies due to the diffusion of counterions into the solution (see SI). While the system as a whole is charge neutral, the non-neutrality of the CPE backbones is consistent with the reported self-doping[70–72] of p-type anionic CPEs. In these systems, the number of electronic charge carriers increases with degree of hydration.[16,17] While significant future work is required to further validate this result, it suggests the potential for future iterations of the CG model used in this work to predict the volumetric capacitance of a CPE morphology, which is a key parameter in predicting transconductance.[73]

In contrast to the minimal impact of the electrostatic potential on electronic site energies in CPEs, electrostatic forces play a significant role in controlling the conformational structure of the fiber-like poor solvent morphologies, which strongly influ-

ence wavefunction delocalization. As seen visually in Figure 6, the HOMOs of good solvent morphologies are localized on individual chains as the through-space coupling is much weaker without poor-solvent induced π-stacking. In contrast, the HOMOs in poor solvent morphologies delocalize across multiple chains via π-stacking and the flattening of intermonomer dihedral angles, as described in previous work.[47] The IPR and DOS of the CPE morphologies (Figure S15 and S16) reveal that through-space coupling, strengthened by anisotropic π-stacking, strongly influences the electronic properties of these morphologies. In good solvent, the DOS tail is 0.1 eV and exhibits no change with concentration while the IPR of the associated MOS was ∼ 10 monomers for all concentrations. In contrast, in poor solvent morphologies the DOS high energy tail was two to three times as long as in good solvent, and the corresponding IPR was four to seven times as large, with both DOS and IPR growing with concentration. When comparing the quenched and compressed morphologies, it appears that both better-connected networks and thicker fibers increase the IPR, but do not have an appreciable impact on the DOS. The sensitivity of MO delocalization to additional onsite energy disorder was probed for selected morphologies, showing that the IPR was reduced by ∼ 15% per 0.1 eV of disorder out to 0.3 eV (Figure S14), but again did not affect qualitative conclusions.

The significant differences in delocalization of the HOMOs strongly affect the electronic mobilities for poor solvent morphologies relative to good solvent morphologies. The large delocalization of HOMOs in poor solvent leads to greater overlap between MOs at larger distances (R_{ij}), increasing the hopping rates and associated electronic mobilities of poor solvent morphologies at all concentrations (Figure 7). The difference in electronic mobilities for the compressed and quenched systems are posited to be due to a combination of network connectivity and fiber thickness, producing more delocalized HOMOs and stronger overlap between MOs. At lower concentrations, the better network connectivity of the quenched morphology appears to improve the mobility by increasing the IPR and providing stronger through-bond coupling between MOs. However, at higher concentrations, the compressed simulation's coarser morphology with fewer and thicker fibers (Figures 4 and S11) produces more delocalized IPRs (Figure S16) and stronger coupling between MOs.

A more in depth analysis of the 20% w/v quenched and 50% w/v compressed morphologies showed that the largest contributions to the electronic mobility result from large rates between nearly-degenerate orbitals at large distances (Figure S17) similar to other organic semiconductor work using time dependent quantum mechanics.[74,75] While there is a stark difference between the electronic mobilities of the good solvent and poor solvent systems that is attributable to the better network structure and improved delocalization resulting from fiber formation, it should be noted that finite size effects likely complicate the detailed comparison of electronic mobility differences between quenched and compressed systems. When the wavefunction is strongly delocalized, the difference between the centroids of different wavefunctions can approach nearly half the box length, requiring careful treatment. Future work will aim to disentangle the differences between poor solvent morphologies at larger length scales.

Fig. 7 Calculated mobility of each morphology for doping levels of 1 dopant (circles) and 10 dopants (squares). Each point is the average mobility along the x, y, and z-axes over 51 snapshots. Error bars represent the standard deviation of the average mobility along the x, y, and z-axes.
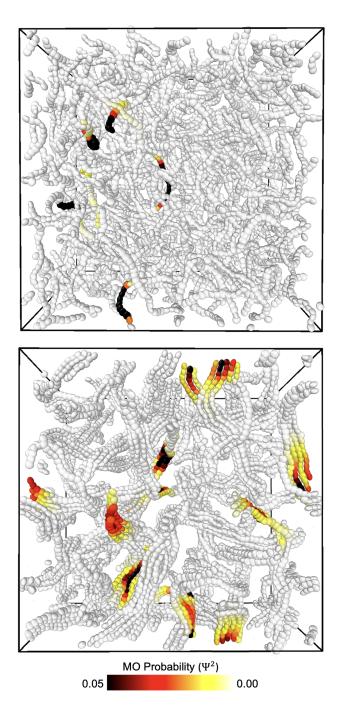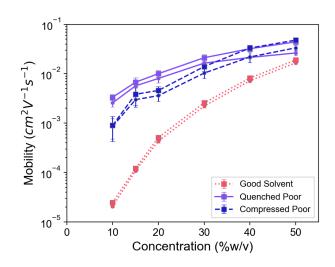

Fig. 6 Wavefunction probability of the top ten highest energy MOs for representative good solvent (top) and poor solvent (bottom) configurations at 20% w/v. Only backbone beads are shown for visual clarity. Some MOs are not visible due to the system density.

2.4 Concentration Dependent Ionic Transport

To provide insight into the use of CPEs as mixed conducting OMIECs,[7] morphology dependent ionic diffusivities were calculated using the Einstein relation. Note that due to the CG nature of simulations, the loss of the polymer and solvent degrees of freedom makes a direct comparison between CG and experimental diffusion rates difficult.

Overall, the diffusion of counterions in CPE systems is nearly linearly dependent on concentration and relatively insensitive to the details of morphology. The diffusion of the counter anions (Figure 8) exhibits a slight non-linear dependence for polymers in good solvent conditions, in agreement with previous work.[76] However, both poor solvent simulations show an identical linear dependence across the range of densities studied ($R^2 > 0.996$). At low concentrations ($< 30\%$ w/v,) the slower diffusion in poor solvent may be due to increased counterion condensation (Figure S7), which increases at higher linear charge densities,[63] a consequence of multiple chains forming a single fiber. At high concentrations ($> 30\%$ w/v), the slower diffusion may be due to confinement of anions to regions of low CPE density (Figure S7), requiring anions to diffuse around the thicker fibers. However, at the semidilute concentrations studied here, the majority of ion transport occurs through the solvent phase, and consequently the small dependence of polymer morphology on the resulting counterion diffusion is observed. Contributions to ion transport from the CPE chain diffusivity was observed to be two orders of magnitude smaller than ion diffusion (Figure S18), with poor solvent diffusivity being approximately three to five times smaller than in good solvent, which is anticipated due to the greater mass of fibers in poor solvent systems.

While this work provides an initial estimation of the structure of CPE morphologies, significant work remains to understand the physical determinants of fiber formation in CPEs, as well as the relationship between simulated and experimental morpholo-
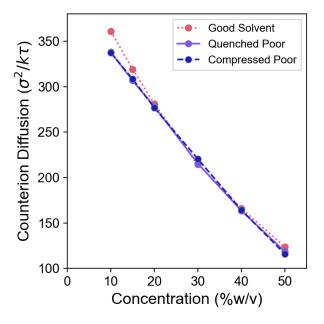
Fig. 8 Ion diffusion constants for good solvent, quenched poor solvent, and compressed poor solvent CPEs as a function of concentration.

gies. While there is copious existing literature advancing the understanding of structure formation in good solvent polyelectrolytes, there is very little work on the corresponding poor solvent polyelectrolyte systems, particularly those exhibiting semiflexible and/or anisotropic interactions. Theoretical works are particularly absent from this area and would be helpful to guide experimental and computational work in future studies. Nonetheless, clear design rules about the nature of poor solvent morphology formation can be deduced from the current work. Fiber formation appears to result from the delicate interplay of short range poor solvent aggregation and longer-range electrostatic repulsion, with the polymer's semiflexibility helping nucleate fiber formation. While the fiber formation in this work is generally consistent with that observed experimentally,[12,14] it is important to note that these experimental systems employ polymers with ~five times larger polymer persistence lengths, and consequently fiber formation occupies larger length scales and is significantly more pronounced. The molecularly detailed view of semidilute poor solvent CPE morphologies in this work suggests the formation of regularly separated multi-chain fibers at the $\sim 10nm$ length scale. This image contrasts with cartoons sometimes presented in the literature showing crystalline and disordered regions in hydrated CPE morphologies, which are likely a gross approximation of the real morphology. Future simulation work employing the CG CPE model will assess the nature of poor solvent morphologies across a broader space of dielectric, short-range intermolecular interactions, and CPE semiflexibilities to provide a more detailed view of the competing physical factors underpinning fiber formation.

A topic that remains unaddressed in the modeling of OMIECs concerns the incorporation of the strong coupling between electronic and ionic degrees of freedom, and the ramifications of this coupling on morphology and charge transport. Specifically, the local electrostatic fields derived from the instantaneous structure of the system will influence both wavefunction delocalization and the likelihood of doping in CPEs, which consequently will modulate the stiffness of the CPE backbone and the electrostatic interactions between ions and holes. In principle, these effects must be treated in a self-consistent fashion, especially for systems operating at high dopant concentrations. This strongly coupled problem has yet to be addressed due to the computational cost of coupling QM changes in wavefunctions with morphology equilibration at the CG resolution. Previous work[30] has distributed the doped hole charges uniformly over the individual polymer chains; while this is a reasonable approximation for computational ease, it does not capture either the physics of delocalization or electrostatically induced disorder. An interesting feature of the models employed in our work relates to the ability to assign master-equation derived holes populations to modulate the local electrostatics of the polymer backbones. In this way, QM-consistent hole populations can be distributed throughout the CPE chains that are consistent with the environmental chain disorder. Significant methodological development is still required to incorporate these effects in a self-consistent, and computationally scalable, manner, but the methods here provide a route to achieving such coupling. As a primary goal of OMIEC modeling concerns accurate estimations of structure, such a framework could be incorporated in a non-dynamical manner utilizing Monte Carlo (MC) schemes in order to provide significant computational advantages. It will be exciting to observe how the ramifications of this included coupling manifest in future work.

Another important issue for OMIECs concerns the development of anisotropic CG models in a fashion that corresponds closely with rigorous bottom-up CG methodologies.[77] Due to the thermodynamic dependence of CG potentials, this was not attempted here due to the broad concentration space examined, but in future work this will constitute an important point of interest. The accuracy of both intramolecular and intermolecular Hamiltonian parameter predictions can also be significantly improved via incorporation of Electronic Coarse-Graining models.[78] The connection of current models to underlying AA models in a statistical mechanically consistent fashion will allow for an assessment of the role of explicit solvent and how results may differ from those incorporating the current implicit solvent model.

Finally, we note that the morphology prediction and transport models introduced in this work are not uniquely the domain of CPEs, and can be straightforwardly adapted to model the broader class of OMIEC materials. Conjugated polymer electrolytes have recently emerged as a promising materials class for OMIECs that imbue ion conductivity using highly polar glycolic side-chains. At present, this class of materials occupies the state-of-the-art of synthetic efforts. Partial charges of the corresponding side-chains could be introduced into the anisotropic CG model and used to study their impact on charge transport. Similar work to this end has recently been conducted by Khot and Savoie,[30,79] though without rigorous connection to the underlying QM Hamiltonian.

3 Conclusions

This work provides the first molecular level view of morphology formation in semi-dilute CPEs and its impact on electronic and ionic mobility. We have employed a QM-informed CG model to study three sets of morphologies spanning good solvent and poor solvent morphologies with different network connectivities. The poor solvent morphologies generated by different annealing procedures result in nearly identical structure factors that show the presence of very regular inter-fiber spacing as characterized by the presence of a harmonic in the PE peak of the partial structure factor. The scaling of this peak with concentration agrees with the scaling in flexible poor solvent PEs (produced by pearl formation), but via a multi-chain fiber formation caused by the semiflexibility and anisotropy of the CPE backbone, which has not previously been studied via theory. We therefore developed an algorithm to measure fiber thickness in these morphologies, and measured the size and number of the networks in each morphology. Despite having very similar structure factors, the two sets of simulations demonstrated distinct differences in network connectivity at low concentrations, and different fiber thicknesses at high concentrations, both of which significantly altered their electronic properties.

The electronic structure of these morphologies was computed using a tight-binding Hamiltonian in a basis of backbone monomer HOMO orbitals to assess how CG morphology impacts electronic properties at large length scales. All monomer energies were determined by the electrostatic potential exerted by the surrounding ions, and their electronic couplings were calculated via dihedral dependent through-bond coupling and orientation dependent through-space coupling. The eigenstates produce by this Hamiltonian showed strong delocalization of the MOs in poor solvent morphologies due to π-stacking induced through-space coupling, with IPRs typically an order of magnitude larger than in the corresponding MOs from good solvent morphologies. The strength of this delocalization was found to be dependent on both the degree of network connectivity at low concentrations, and the fiber thickness at high concentrations. The electronic mobility of these morphologies were then calculated using semiclassical rate theory and equilibrium populations calculated using a mean field master equation approach. The calculated mobilities spanned three orders of magnitude, with each set of simulations exhibiting a unique concentration dependence. In contrast, the ionic diffusivity appears relatively insensitive to the details of polymer morphology at the studied concentrations, with minute perturbations due to differences in counterion condensation in the aggregated fibers. The overarching conclusion of this work supports that the electronic mobility of CPE morphologies depends most strongly on the degree of MO delocalization, which can be tailored by the CPE morphologies network connectivity and fiber thickness. The precise ability to tune these morphologies, and the resulting ion-electron transport properties, as a function of dielectric constant, solvent quality, and chain flexibility motivates future work at the interface of theory, computation, and experiment.

Conflicts of interest

Acknowledgements

Notes and references

1 B. Liu and G. C. Bazan, *Conjugated Polyelectrolytes: Fundamentals and Applications*, Wiley-VCH Verlag GmbH Co. KGaA, 2012.

2 H. Jiang, P. Taranekar, J. Reynolds and K. Schanze, *Angew. Chem. Int. Ed.*, 2009, **48**, 4300–4316.

3 R. C. So and A. C. Carreon-Asok, *Chem. Rev.*, 2019, **119**, 11442–11509.

4 M. R. Pinto and K. S. Schanze, *Proceedings of the National Academy of Sciences*, 2004, **101**, 7505–7510.

5 A. Gumyusenge, *Acc. Mater. Res.*, 2022, **3**, 669–671.

6 S. Inal, J. Rivnay, A.-O. Suiu, G. G. Malliaras and I. McCulloch, *Acc. Mater. Res.*, 2018, **51**, 1368–1376.

7 B. D. Paulsen, K. Tybrandt, E. Stavrinidou and J. Rivnay, *Nat. Mater.*, 2020, **19**, 13–26.

8 J. Tropp, A. S. Mehta, A. Ji, A. Surendran, R. Wu, E. A. Schafer, M. M. Reddy, S. P. Patel, A. J. Petty and J. Rivnay, *Chem. Mater.*, 2022.

9 J. Chung, A. Khot, B. M. Savoie and B. W. Boudouris, *ACS Macro Lett.*, 2020, **9**, 646–655.

10 A. P.-Z. Clark, C. Shi, B. C. Ng, J. N. Wilking, A. L. Ayzner, A. Z. Stieg, B. J. Schwartz, T. G. Mason, Y. Rubin and S. H. Tolbert, *ACS nano*, 2013, **7**, 962–977.

11 Y. D. Zaroslov, V. Gordeliy, A. Kuklin, A. Islamov, O. Philippova, A. Khokhlov and G. Wegner, *Macromolecules*, 2002, **35**, 4466–4471.

12 R. C. Huber, A. S. Ferreira, J. C. Aguirre, D. Kilbride, D. B. Toso, K. Mayoral, Z. H. Zhou, N. Kopidakis, Y. Rubin, B. J. Schwartz *et al.*, *J. Phys. Chem. B*, 2016, **120**, 6215–6224.

13 S. P. Danielsen, G. E. Sanoja, S. R. McCuskey, B. Hammouda, G. C. Bazan, G. H. Fredrickson and R. A. Segalman, *Chem. Mater.*, 2018, **30**, 1417–1426.

14 S. P. Danielsen, B. J. Thompson, G. H. Fredrickson, T.-Q. Nguyen, G. C. Bazan and R. A. Segalman, *Macromolecules*, 2022, **55**, 3437–3448.

15 R. J. Vázquez, G. Quek, S. R. McCuskey, L. Llanes, B. Kundukad, X. Wang and G. C. Bazan, *J. Mater. Chem. A*, 2022, **10**, 21642–21649.

16 G. L. Grocke, B. X. Dong, A. D. Taggart, A. B. Martinson, J. Niklas, O. G. Poluektov, J. W. Strzalka and S. N. Patel, *ACS Poly. Au*, 2022, **2**, 275–286.

17 M. Wieland, C. Dingler, R. Merkle, J. Maier and S. Ludwigs, *ACS Appl. Mater. Interfaces*, 2020, **12**, 6742–6751.

18 D. Rawlings, D. Lee, J. Kim, I.-B. Magdau, G. Pace, P. M. Richardson, E. M. Thomas, S. P. Danielsen, S. H. Tolbert, T. F. Miller III *et al.*, *Chem. Mater.*, 2021, **33**, 6464–6474.

19 R. Merkle, P. Gutbrod, P. Reinold, M. Katzmaier, R. Tkachov, J. Maier and S. Ludwigs, *Polymer*, 2017, **132**, 216–226.

20 Y. Wan, F. Ramirez, X. Zhang, T.-Q. Nguyen, G. C. Bazan and G. Lu, *npj Comput. Mater.*, 2021, **7**, 1–9.

21 Y. Wan, X. Zhang, G. C. Bazan, T.-Q. Nguyen and G. Lu, *Adv. Funct. Mater.*, 2022, 2209394.

22 J. Sjoqvist, M. Linares, K. V. Mikkelsen and P. Norman, *J. Phys. Chem. A*, 2014, **118**, 3419–3428.

23 G. Hostnik, C. Podlipnik, G. Mériguet and J. Cerar, *Macromolecules*, 2020, **53**, 1119–1128.

24 H. Oberhofer, K. Reuter and J. Blumberger, *Chemical reviews*, 2017, **117**, 10319–10357.

25 C. M. Isborn, B. D. Mar, B. F. Curchod, I. Tavernelli and T. J. Martinez, *The Journal of Physical Chemistry B*, 2013, **117**, 12189–12201.

26 R. Alessandri, J. J. Uusitalo, A. H. de Vries, R. W. A. Havenith and S. J. Marrink, *J. Am. Chem. Soc.*, 2017, **139**, 3697–3705.

27 D. Hu, K. Wong, B. Bagchi, P. J. Rossky and P. F. Barbara, *Nature*, 2000, **405**, 1030–1033.

28 M. Ricci, O. M. Roscioni, L. Querciagrossa and C. Zannoni, *Phys. Chem. Chem. Phys.*, 2019, **21**, 26195–26211.

29 C. Greco, A. Melnyk, K. Kremer, D. Andrienko and K. C. Daoulas, *Macromolecules*, 2019, **52**, 968–981.

30 A. Khot and B. M. Savoie, *Macromolecules*, 2021, **54**, 4889–4901.

31 S. A. Mollinger, A. Salleo and A. J. Spakowitz, *ACS Cent. Sci.*, 2016, **2**, 910–915.

32 P. E. Rudnicki, Q. MacPherson, L. Balhorn, B. Feng, J. Qin, A. Salleo and A. J. Spakowitz, *Macromolecules*, 2019, **52**, 8932–8939.

33 M. Matta, R. Wu, B. D. Paulsen, A. J. I. Petty, R. Sheelamanthula, I. McCulloch, G. C. Schatz and J. Rivnay, *Chemistry of Materials*, 2020, **32**, 7301–7308.

34 M. Matta, A. Pezzella and A. Troisi, *J. Phys. Chem. Lett.*, 2020, **11**, 1045–1051.

35 S. Moro, N. Siemons, O. Drury, D. A. Warr, T. A. Moriarty, L. M. A. Perdigão, D. Pearce, M. Moser, R. K. Hallani, J. Parker, I. McCulloch, J. M. Frost, J. Nelson and G. Costantini, *ACS Nano*, 2022, **16**, 21303–21314.

36 T. Wang and J.-L. Brédas, *J. Am. Chem. Soc.*, 2021, **143**, 1822–1835.

37 V. Bhat, P. Sornberger, B. S. S. Pokuri, R. Duke, B. Ganapathysubramanian and C. Risko, *Chem. Sci.*, 2023, **14**, 203–213.

38 L. Zhu, E.-G. Kim, Y. Yi and J.-L. Brédas, *Chemistry of Materials*, 2011, **23**, 5149–5159.

39 M. Comin, V. Lemaur, A. Giunchi, D. Beljonne, X. Blase and G. D'Avino, *J. Mater. Chem. C*, 2022, **10**, 13815–13825.

40 D. Moia, A. Giovannitti, A. A. Szumska, I. P. Maria, E. Rezasoltani, M. Sachs, M. Schnurr, P. R. Barnes, I. McCulloch and J. Nelson, *Energy Environ. Sci.*, 2019, **12**, 1349–1357.

41 G. Gryn'ova, K.-H. Lin and C. Corminboeuf, *Journal of the American Chemical Society*, 2018, **140**, 16370–16386.

42 A. V. Volkov, K. Wijeratne, E. Mitraka, U. Ail, D. Zhao, K. Tybrandt, J. W. Andreasen, M. Berggren, X. Crispin and I. V. Zozoulenko, *Adv. Funct. Mater.*, 2017, **27**, 1700329.

43 I. Zozoulenko, J. F. Franco-Gonzalez, V. Gueskine, A. Mehandzhiyski, M. Modarresi, N. Rolland and K. Tybrandt, *Macromolecules*, 2021, **54**, 5915–5934.

44 N. Rolland, M. Modarresi, J. F. Franco-Gonzalez and I. Zozoulenko, *Comput. Mater. Sci.*, 2020, **179**, 109678.

45 W. Michaels, Y. Zhao and J. Qin, *Macromolecules*, 2021, **54**, 3634–3646.

46 W. Michaels, Y. Zhao and J. Qin, *Macromolecules*, 2021, **54**, 5354–5365.

47 D. M. Friday and N. E. Jackson, *Macromolecules*, 2022, **55**, 1866–1877.

48 S. Plimpton, *J. Comp. Phys.*, 1995, **117**, 1–19.

49 W. M. Brown, M. K. Petersen, S. J. Plimpton and G. S. Grest, *J. Chem. Phys.*, 2009, **130**, 044901.

50 R. Berardi, C. Fava and C. Zannoni, *Chem. Phys. Lett.*, 1998, **297**, 8–14.

51 B. Kuei and E. D. Gomez, *Soft Matter*, 2017, **13**, 49–67.

52 A. E. Cohen, N. E. Jackson and J. J. de Pablo, *Macromolecules*, 2021, **54**, 3780–3789.

53 B. J. Boehm, C. R. McNeill and D. M. Huang, *Nanoscale*, 2022, **14**, 18070–18086.

54 J. H. Bombile, M. J. Janik and S. T. Milner, *Phys. Chem. Chem. Phys.*, 2016, **18**, 12521–12533.

55 J. Vura-Weis, M. A. Ratner and M. R. Wasielewski, *J. Am. Chem. Soc.*, 2010, **132**, 1738–1739.

56 P. F. Barbara, T. J. Meyer and M. A. Ratner, *The Journal of Physical Chemistry*, 1996, **100**, 13148–13168.

57 R. P. Fornari and A. Troisi, *Phys. Chem. Chem. Phys.*, 2014, **16**, 9997–10007.

58 J. C. Maier and N. E. Jackson, *Macromolecules*, 2021, **54**, 7060–7069.

59 Z. Yu, D. Smith, A. Saxena, R. Martin and A. Bishop, *Phys. Rev. B*, 2001, **63**, 085202.

60 V. Arkhipov, E. Emelianova, P. Heremans and H. Bässler, *Phys. Rev. B*, 2005, **72**, 235202.

61 A. Yethiraj, *Phys. Rev. Lett.*, 1997, **78**, 3789.

62 M. J. Stevens and K. Kremer, *J. Chem. Phys.*, 1995, **103**, 1669–1690.

63 A. V. Dobrynin, *Polymer*, 2020, **202**, 122714.

64 A. Stukowski, *Model. Simul. Mater. Sci. Eng*, 2010, **18**,.

65 B. D. Ermi and E. J. Amis, *Macromolecules*, 1997, **30**, 6937–6942.

66 H. J. Limbach, C. Holm and K. Kremer, Macromolecular Symposia, 2004, pp. 43–54.

67 B. M. Savoie, K. L. Kohlstedt, N. E. Jackson, L. X. Chen, M. Olvera de la Cruz, G. C. Schatz, T. J. Marks and M. A. Ratner, *Proc. Natl. Acad. Sci.*, 2014, **111**, 10055–10060.

68 M. A. Webb, B. M. Savoie, Z.-G. Wang and T. F. Miller III, *Macromolecules*, 2015, **48**, 7346–7358.

69 L. McInnes, J. Healy and J. Melville, *arXiv preprint arXiv:1802.03426*, 2018.

70 W. Cai, C. Musumeci, F. N. Ajjan, Q. Bao, Z. Ma, Z. Tang and O. Inganäs, *J. Mater. Chem. A*, 2016, **4**, 15670–15675.

71 C.-K. Mai, H. Zhou, Y. Zhang, Z. B. Henson, T.-Q. Nguyen, A. J. Heeger and G. C. Bazan, *Angew. Chem.*, 2013, **52**, 12874–12878.

72 D. X. Cao, D. Leifert, V. V. Brus, M. S. Wong, H. Phan, B. Yurash, N. Koch, G. C. Bazan and T.-Q. Nguyen, *Mater. Chem. Front.*, 2020, **4**, 3556–3566.

73 J. Rivnay, S. Inal, A. Salleo, R. M. Owens, M. Berggren and G. G. Malliaras, *Nat. Rev. Mater.*, 2018, **3**, 1–14.

74 S. Giannini, A. Carof, M. Ellis, H. Yang, O. G. Ziogos, S. Ghosh and J. Blumberger, *Nature communications*, 2019, **10**, 1–12.

75 S. Giannini and J. Blumberger, *Accounts of Chemical Research*, 2022, **55**, 819–830.

76 J. Snyder, M. Ratner and D. Shriver, *J. Electrochem. Soc.*, 2001, **148**, A858.

77 H. T. L. Nguyen and D. M. Huang, *J. Chem. Phys.*, 2022, **156**, 184118.

78 J. C. Maier and N. E. Jackson, *J. Chem. Phys.*, 2022, **157**, 174102.

79 A. Khot and B. M. Savoie, *J. Polym. Sci.*, 2022, **60**, 610–620.